Confirmation of ξ^1 CMa's ultra-slow rotation: magnetic polarity reversal and a dramatic change in magnetospheric UV emission lines

C. Erba [1]*, M. E. Shultz,[1] V. Petit [1], A. W. Fullerton,[2] H. F. Henrichs,[3] O. Kochukhov [4], T. Rivinius[5] and G. A. Wade[6]

[1]*Department of Physics and Astronomy, Bartol Research Institute, University of Delaware, Newark, DE 19716, USA*
[2]*Space Telescope Science Institute, Baltimore, MD 21218, USA*
[3]*Anton Pannekoek Institute for Astronomy, University of Amsterdam, Science Park 904, NL-1098 XH Amsterdam, the Netherlands*
[4]*Department of Physics and Astronomy, Uppsala University, Box 516, SE-751 20 Uppsala, Sweden*
[5]*European Organisation for Astronomical Research in the Southern Hemisphere (ESO), Casilla 19001, Santiago 19, Chile*
[6]*Department of Physics and Space Science, Royal Military College of Canada, PO Box 17000, Station Forces, Kingston, ON K7K 0C6, Canada*

ABSTRACT

The magnetic β Cep pulsator ξ^1 CMa has the longest rotational period of any known magnetic B-type star. It is also the only magnetic B-type star with magnetospheric emission that is known to be modulated by both rotation and pulsation. We report here the first unambiguous detection of a negative longitudinal magnetic field in ξ^1 CMa ($\langle B_z \rangle = -87 \pm 2$ G in 2019 and $\langle B_z \rangle = -207 \pm 3$ G in 2020), as well as the results of ongoing monitoring of the star's Hα variability. We examine evidence for deviation from a purely dipolar topology. We also report a new *HST* UV spectrum of ξ^1 CMa obtained near magnetic null that is consistent with an equatorial view of the magnetosphere, as evidenced by its similarity to the UV spectrum of β Cep obtained near maximum emission. The new UV spectrum of ξ^1 CMa provides additional evidence for the extremely long rotation period of this star via comparison to archival data.

Key words: techniques: polarimetric – stars: early-type – stars: individual: ξ^1 CMa – stars: magnetic field – stars: massive – ultraviolet: stars.

1 INTRODUCTION

Approximately 10 per cent of O- and B-type stars host large-scale strong surface magnetic fields with strengths on the order of 1 kG (Morel et al. 2015; Wade et al. 2016; Grunhut et al. 2017; Petit et al. 2019) that have a significant effect on stellar evolution (Petit et al. 2017; Keszthelyi et al. 2019). By trapping wind plasma within closed magnetic loops, these magnetospheres reduce the net mass-loss rate from the stellar surface (ud-Doula & Owocki 2002) and contribute to rapid stellar angular momentum loss (magnetic braking; ud-Doula, Owocki & Townsend 2009). In extreme cases, this can lead to an essentially non-rotating star (e.g. HD 108, with a rotation period of ∼55 yr; Nazé et al. 2010; Shultz & Wade 2017).

Among this subpopulation of extremely slow rotators, the magnetic β Cep pulsator ξ^1 CMa (HD 46328, B0.5 IV) stands out due to its remarkable characteristics. The magnetic detection, first reported by Hubrig et al. (2006) and later confirmed by Silvester et al. (2009), identified the strongest surface magnetic field measured for any B0 star (∼1 kG). Indeed, the star's magnetic field has not yet been fully characterized, since a complete rotation period of ξ^1 CMa has not yet been observed. To date, longitudinal magnetic field measurements of the star span approximately 20 yr, with the earliest recorded observations from the year 2000 (Shultz et al. 2017). Using FORS2 and SOFIN spectropolarimetric data, Hubrig et al. (2011) and

Järvinen et al. (2018) claimed a much shorter rotation period of 2.17937 d. These findings were challenged by Shultz et al. (2017, 2018c), who showed that only an extraordinarily long rotation period of ∼30 yr was consistent with the high-resolution spectropolarimetric data sets obtained with ESPaDOnS. ξ^1 CMa therefore exhibits the longest rotation period of any known magnetic B-type star (Shultz et al. 2017, 2018b).

ξ^1 CMa also shows evidence for departures from a purely dipolar magnetic topology. Shultz et al. (2018c) reported a crossover signature at magnetic null which, given the negligible $v\sin i$ implied by the extremely long rotation period, could only be explained by the interaction of multipolar components of the surface magnetic field with radial velocity (RV) perturbations introduced by radial pulsation.

ξ^1 CMa is classified as a β Cep pulsator, displaying monoperiodic radial pulsations with a ∼5-h period (Saesen, Briquet & Aerts 2006). This pulsational modulation is observed in the X-ray light curve (Oskinova et al. 2014) and in the Hα emission (Shultz et al. 2017), a phenomenon unique among hot magnetic stars. Furthermore, the star's Hα emission exhibits characteristics that suggest it originates within a dynamical magnetosphere (Shultz et al. 2017), a magnetospheric class characteristic of slow rotators. Such a phenomenon is more typically observed within the (more luminous) magnetic O-type star population (Petit et al. 2013) and diverges from all other Hα-bright magnetic B-type stars, which have rapid rotation and are observed to have optical emission consistent with a centrifugal magnetosphere (Petit et al. 2013; Shultz et al. 2019b).

* E-mail: cerba@udel.edu

ξ^1 CMa may therefore be an important transitional object located in the divide between the magnetic O- and B-type stars.

All hot stars show high-ionization ultraviolet (UV) lines caused by outflowing winds, as apparent from their P-Cygni profiles. For non-magnetic stars, these profiles show strong variability pre-dominantly in their absorption component (e.g. Massa et al. 1995; Kaper et al. 1996, 1999), which is much more sensitive to changes in the line-of-sight column density than the emission part (which is caused by scattering in all directions). In contrast, the wind-sensitive resonance line profiles of the confirmed magnetic B stars, in particular the He-peculiar stars (e.g. Shore 1987; Wade et al. 2000; Shultz et al. 2019a), differ significantly in two aspects: the variability extends over the full P-Cygni profile (including the emission) and the overall shape of the profile is rotationally modulated. Galleries of the UV C IV $\lambda\lambda 1548$, 1550 line behaviour in different types of magnetic B stars have been presented by Henrichs (2001) and Henrichs et al. (2012). These two properties therefore serve as the strongest indirect indicator of magnetic B stars (Henrichs et al. 1993) and were used to predict the presence of a magnetic field in the B1 IV star β Cep (HD 205 021; Henrichs et al. 2000, 2013; Donati et al. 2001). A similar prediction from the UV-line behaviour was made for the β Cep-variable He-strong star V2052 Oph (HD 163 472, B2 IV-V; Henrichs et al. 1998) after which the field was discovered by Neiner et al. (2003b). This approach also led to the discovery of the magnetic field of the slowly pulsating B star ζ Cas (HD 3360, B2 IV; Neiner et al. 2003a) and the He-strong star σ Lup (HD 127 381, B1/B2 V; Henrichs et al. 2012).

It should be emphasized, however, that the target list to search for magnetic B stars was originally based on the abundance study by Gies & Lambert (1992). The authors found a number of near main-sequence B stars (including ξ^1 CMa, β Cep, and ζ Cas) with an overabundance of nitrogen, which was later confirmed by Morel et al. (2006). Indeed, the UV C IV profile of ξ^1 CMa is very anomalous for its spectral type (see fig. 3 of Schnerr et al. 2008), which strongly supports the presence of a magnetic field in this star. However, UV rotational modulation has not yet been detected for ξ^1 CMa, since the only reported UV spectra to date are all consistent with observations of the star near a state of maximum emission (Schnerr et al. 2008; Shultz et al. 2017).

In this paper, we provide an updated spectropolarimetric data set through the year 2020 and confirm the first definite detection of a negative longitudinal magnetic field in ξ^1 CMa. We report the results of continued monitoring of the star's unique Hα emission, and we present the first new UV spectrum of ξ^1 CMa obtained in approximately 40 yr. In Section 2, we describe the observational data sets used in our work. The magnetic analysis is covered in Section 3. The Hα and UV magnetospheric diagnostics are presented in Section 4. Finally, we discuss our conclusions in Section 5.

2 OBSERVATIONS

2.1 ESPaDOnS spectropolarimetry

A total of 19 high-resolution ($R \sim 68\,000$) spectropolarimetric sequences were obtained between 2019 March 15 and 22 with ESPaDOnS at the Canada–France–Hawaii Telescope (CFHT). Additional seven ESPaDOnS sequences were obtained between 2020 November 29 and 2020 December 08.[1] The log of these observations is provided in Table 1. ESPaDOnS is an echelle spectropolarimeter that covers a wavelength range of approximately 3700–10 500 Å

[1]Programme codes 19AC20 and 20BC16.

Table 1. Table of radial velocity (RV) uncertainties extracted from the full spectropolarimetric sequences and longitudinal magnetic field ($\langle B_z \rangle$) measurements obtained during the 2019–2020 epochs. The measurement of the null spectrum ($\langle N_z \rangle$) is also reported for each date. Pulsation phases are calculated using the nonlinear ephemeris from Shultz et al. (2017).

HJD – 2 450 000	Pulsation phase	RV (km s^{-1})	$\langle B_z \rangle$ (G)	$\langle N_z \rangle$ (G)	Peak S/N
8557.76842	0.94	40.7	-105 ± 9	0 ± 9	635
8557.77404	0.97	41.1	-99 ± 9	5 ± 9	629
8557.83912	0.28	16.4	-77 ± 10	-8 ± 10	617
8557.84474	0.31	14.0	-90 ± 9	-15 ± 9	676
8557.85042	0.33	11.9	-93 ± 9	-9 ± 9	658
8559.76381	0.46	7.5	-87 ± 8	-18 ± 8	717
8559.76894	0.49	7.9	-79 ± 8	-5 ± 8	666
8559.78451	0.56	10.7	-79 ± 8	7 ± 8	696
8559.78985	0.59	12.2	-81 ± 9	-11 ± 9	640
8559.79528	0.61	14.1	-95 ± 9	6 ± 9	622
8559.81285	0.70	21.5	-87 ± 8	7 ± 8	653
8559.82521	0.76	27.3	-80 ± 9	-2 ± 9	673
8560.71412	1.00	40.6	-102 ± 8	8 ± 8	743
8560.72028	0.03	39.4	-92 ± 8	-1 ± 8	768
8560.72525	0.05	38.0	-90 ± 8	2 ± 8	762
8560.76297	0.23	21.0	-77 ± 8	-1 ± 8	764
8563.74440	0.46	7.5	-79 ± 7	-10 ± 7	823
8564.84783	0.72	24.0	-80 ± 7	-6 ± 7	786
8564.85276	0.74	26.3	-86 ± 7	-1 ± 7	797
9183.05041	0.46	7.9	-208 ± 8	-6 ± 8	970
9184.00041	0.99	39.8	-225 ± 10	5 ± 10	759
9187.02585	0.43	7.7	-196 ± 8	4 ± 7	1050
9190.06572	0.94	40.1	-210 ± 8	4 ± 8	995
9190.96634	0.23	19.7	-213 ± 8	-3 ± 8	1017
9191.93719	0.86	36.9	-199 ± 7	-3 ± 7	1004
9192.02958	0.31	13.1	-206 ± 8	-1 ± 8	1036

across 40 orders. Each observation is comprised of four subexposures, each with a 70 s duration, from which four Stokes I spectra, one Stokes V spectrum, and two null (N) spectra are calculated (Donati et al. 1997). The null spectra are extracted from the four subexposures according to the method outlined in Donati et al. (1997), such that any inherent polarization of the source is cancelled out. The data were reduced using Upena, the standard pipeline for ESPaDOnS data from CFHT. Upena utilizes the Libre-ESpRIT software developed by Donati et al. (1997). A detailed description of the reduction and analysis of ESPaDOnS data can be found in Wade et al. (2016). The peak signal-to-noise (S/N) ratio of the Stokes V spectra per 1.8 km s^{-1} pixel ranges between 617 and 1050. The mean peak S/N ratio per pixel of the Stokes I spectra is approximately 500 (so the data quality is comparable to previous observing seasons).

We calculated RV measurements (Table A1) from the individual subexposures of the spectropolarimetric sequences, following the multiline procedure described by Shultz et al. (2017). The RVs from the 2019 observations were published by Wade et al. (2020). To calculate pulsation phase, we adopt the nonlinear ephemeris ($P_0 = 0.2095763(1)$ d and $\dot{P} = 0.0096(5)$ s yr^{-1}) from Shultz et al. (2017), consistent with the short-term period evolution described by Wade et al. (2020).

2.2 *HST* ultraviolet spectroscopy

Forty-two ultraviolet spectra of ξ^1 CMa were obtained during a monitoring campaign with the Space Telescope Imaging Spectrograph (STIS) onboard the *Hubble Space Telescope* (*HST*) in 2017 February as part of Cycle 24 GO Program 14657 (PI: Oskinova). These data were retrieved from the Mikulski Archive for Space

Telescopes (MAST) data base.[2] The observations were broken into six visits that occurred over six consecutive orbits, with a gap of ~64 min between the last exposure of one visit and the start of the first exposure of the next visit. The total time coverage amounted to 8.45 h, which spanned 1.68 cycles of the ~0.209 d pulsational period of ξ^1 CMa. Table B1 provides a journal of these observations.

The observing sequence for each visit began with a standard target acquisition to center ξ^1 CMa accurately in the 0.3X0.05ND aperture of STIS. The attenuation provided by this aperture was required to mitigate the brightness of the source. Following an 'auto-wavecal' exposure of the internal Pt-Cr/Ne wavelength calibration lamp, seven consecutive exposures were obtained with the ACCUM mode of the far-ultraviolet MAMA photon-counting detector and the E140M grating. The exposure time for each of the first six spectra was 228 s, but only 218 s for the final spectrum to accommodate orbital constraints. In either case, the degree of 'phase smearing' of the pulsational period is negligible. The E140M grating provided wavelength coverage from 1140 Å (order 129) to 1709 Å (order 87) with resolving power of ~46 000. The S/N ratio was ~6 pixel^{-1} in the vicinity of 1495 Å.

The spectra were uniformly processed with version 3.4.2 (2018 January 19) of the standard CALSTIS calibration pipeline (Sohn et al. 2019), which included steps to: (1) correct for detector nonlinearity; (2) subtract contributions from dark current; (3) apply a flat-field to mitigate pixel-to-pixel sensitivity variations; (4) correct for geometric distortion; and (5) determine and apply corrections to the wavelength zero-point. After a 1D spectrum was extracted for each order, contributions due to scattered light were removed and both the dispersion solution and photometric calibration were applied. As a final step, we stitched together these extracted, calibrated spectra by matching the flux levels in the regions of overlap between successive orders to create a single, merged spectrum for each exposure.

The individual spectra were normalized and coadded into a single spectrum to increase the S/N ratio. Pulsation-induced variations in the spectra are small compared to the variability due to rotational modulation, therefore a small amount of phase smearing in the coadded spectrum is inconsequential to the purpose of this work (see Section 4.2 below).

2.3 Previously published data sets

We include several previously published data sets in our analysis, described in the sections below.

2.3.1 *ESPaDOnS spectropolarimetry*

A total of 64 high-resolution spectropolarimetric sequences were obtained with ESPaDOnS at CFHT between 2008 January 23 and 2018 July 07 (Silvester et al. 2009; Shultz et al. 2017, 2018c). A detailed description of the observations from 2008 to 2017 was given by Shultz et al. (2017). Observations from the year 2018 were discussed by Shultz et al. (2018c).

2.3.2 *MuSiCoS spectropolarimetry*

Three high-resolution ($R \sim 35\,000$) optical Stokes V spectra were obtained between 2000 February 5 and 11 using the MuSiCoS spec-tropolarimeter, which was mounted on the Bernard Lyot Telescope

(TBL) at the Pic du Midi Observatory (Baudrand & Bohm 1992; Donati et al. 1999). Details about the reduction and analysis of these data were given by Shultz et al. (2017).

2.3.3 *CORALIE spectroscopy*

A large number of spectra (401) were obtained using the CORALIE optical spectrograph between 2000 February 17 and 2004 October 5. CORALIE is mounted at the Leonhard Euler Telescope at La Silla observatory, and is operated by the Geneva Observatory (Queloz et al. 2000, 2001). These data were first analysed and published by Saesen et al. (2006), and were used again by Shultz et al. (2017).

2.3.4 IUE *ultraviolet spectroscopy*

ξ^1 CMa was observed 13 times by the Interstellar Ultraviolet Explorer (*IUE*) in high-resolution ($\lambda/\Delta\lambda \sim 20\,000$) mode using the Short Wavelength Prime (SWP) camera. The S/N of all observations is approximately 20. The first observation was acquired in 1978, and the remaining 12 about 142 d later, covering one pulsation cycle with regular phase intervals. The data were reduced with the New Spectral Image Processing System (NEWSIPS; Nichols & Linsky 1996) and were retrieved from the MAST archive.[3] We used the absolute calibrated flux, discarded pixels flagged as anomalous, and merged individual spectral orders at the wavelengths where the flux uncertainties of adjacent orders overlapped. The spectra were normalized and coadded into a single spectrum. Since the pulsation amplitude is much smaller than the line widths, pulsation smearing is negligible.

We also utilized seven spectra of β Cep obtained with *IUE*/SWP between 1979 February 24 and 1995 February 14. The data were reduced and post-processed using the same procedure as described above. Since the rotational period of β Cep is known (12 d; Henrichs et al. 1993, 2013), we selected the spectra at maximum emission (rotation phase $\phi_{rot} = 0.0$) and at minimum emission ($\phi_{rot} = 0.25$) for comparison to the UV spectra of ξ^1 CMa. For the N V $\lambda\lambda$1238, 1242 spectral line, in order to increase the S/N ratio, we selected spectra within the range $\phi_{rot} = 0.0 \pm 0.025$. For each group, the spectra were normalized and coadded into a single spectrum.

3 MAGNETIC ANALYSIS

In order to increase the S/N ratio of the Zeeman signatures present in the Stokes V profiles of ξ^1 CMa, we extracted mean line profiles using the least-squares deconvolution (LSD; Donati et al. 1997) method. We applied the same custom Vienna Atomic Line Database (VALD3; Piskunov et al. 1995; Ryabchikova et al. 1997, 2015; Kupka et al. 1999, 2000) line mask as Shultz et al. (2017, 2018c). The LSD profiles are extracted with weights corresponding to a line with $d = 0.1$, $g = 1.2$, and $\lambda = 500$ nm. The individual line profiles were shifted to their respective rest velocities by subtracting the measured radial velocities from Table 1. We calculated False Alarm Probabilities (FAPs; Donati et al. 1997), which are used to assess detection flag statistics. We used a range of ± 30 km s^{-1} around line center. All of the Stokes V profiles yield definite detections (DD; FAP $<10^{-5}$), and all of the null profiles produce non-detections (ND; FAP $>10^{-3}$). This is consistent with previous measurements of $\langle B_z \rangle$ and $\langle N_z \rangle$; DDs in the null profiles do occur in ξ^1 CMa, but only when $\langle B_z \rangle$ is high (Shultz et al. 2017).

---

[2] Access to the MAST data base is available at https://archive.stsci.edu/.

[3] Available at https://archive.stsci.edu/iue/.

Fig. 1 shows the Stokes *V* and Stokes *I* profiles from the 2019 and 2020 spectropolarimetric data sets (new to this paper), compared with profiles from earlier observational data sets (previously published by Shultz et al. 2017, 2018c). The 2019 observations provide the first unambiguous measurement of a negative longitudinal magnetic field, confirming the inference from the MuSiCoS data set (formally a non-detection) that both magnetic poles are visible over a rotational cycle. This can also be seen in the reversal of the Stokes *V* signature in the LSD profiles between the 2017 and 2019 epochs.

The Stokes *V* profiles show similar morphologies and polarities, and yield similar longitudinal fields, within a given year, consistent with expectations for a long rotation period. The 2019 observations match the amplitude (with reversed polarity) of the corresponding observations in the 2017 data set that were obtained at the same pulsational phase. Furthermore, the amplitudes of the 2020 profiles are similar to those in the 2014 data set. Positive Zeeman signatures are seen in the 2014 and 2017 Stokes *V* profiles, while negative Zeeman signatures appear in the 2019 and 2020 profiles. Such behaviour is consistent with what would be expected in the case of a long rotational period, with the longitudinal field crossing magnetic null in 2018 (Shultz et al. 2018c). Any short-term variability of the Stokes *V* profiles is therefore best explained by pulsation, while the long-term variability is due to rotation.

The 2019 Stokes *V* profiles near pulsation phase $\phi_p = 0$ have unusual, non-antisymmetric shapes, which are distinct from the observations obtained at pulsation phases just above and below that value. These unusual profiles are shown in Fig. 2 (red lines), which provides a close-up view of the highlighted panels in Fig. 1. There is no significant change in the shape of the 2019 Stokes *I* profiles for pulsation phases near $\phi_p = 0$. Additionally, the unusual shape of the Stokes *V* profiles is not seen in the 2017 data set (Fig. 2, black lines) which also has closely spaced observations in the same range of pulsation phases.

Shultz et al. (2018c) reported the presence of crossover signatures[4] that vary coherently with pulsation phase in the 2018 Stokes *V* profiles, which are not anticipated given the negligible $v \sin i$ inferred from ξ^1 CMa's long rotation period. The authors found that such crossover signatures are the result of a 'radial crossover' effect, arising from the interaction between the velocity field introduced by radial pulsations and the complex topology of the magnetic field. It is therefore possible that the change in the shape of the 2019 Stokes *V* profile also results from this interaction. Furthermore, because this abnormality is absent from the 2017 Stokes *V* profiles, there may be an as-yet unobserved asymmetry in the topology of the field between the north and south magnetic poles.

The longitudinal magnetic field $\langle B_z \rangle$ provides a quantitative measure of the line-of-sight field strength (Mathys 1989). Accordingly, we measured $\langle B_z \rangle$ using an integration range of ± 30 km s^{-1} around line centre, following the procedure from Shultz et al. (2017), and the LSD scaling mentioned above. The $\langle B_z \rangle$ measurement for each polarimetric sequence in the new epoch is reported in Table 1. All of the $\langle B_z \rangle$ values are negative: the error bar-weighted mean of the longitudinal field from the 2019 data set, $\langle B_z \rangle = -87 \pm 2$ G, decreases to $\langle B_z \rangle = -207 \pm 3$ G in the 2020 data set. Null profile measurements are all consistent with zero: the weighted mean of the 2019 null profiles is $\langle N_z \rangle = -3 \pm 2$ G. Similarly, the weighted

mean of the 2020 null profiles is $\langle N_z \rangle = -1 \pm 3$ G. The mean error in the individual $\langle B_z \rangle$ measurements is consistent with the standard deviation of $\langle B_z \rangle$ within each observational epoch (about 8 G in all cases).

Fig. 3(a) shows the $\langle B_z \rangle$ curve with a sinusoidal fundamental harmonic fit (black solid line), illustrating what would be expected for a purely dipolar field. From this fit, the sum of the inclination and obliquity angles $i + \beta$ can be constrained (Preston 1967). We calculated Preston's r parameter using the Monte Carlo sampler from Shultz et al. (2019b), setting the mean $\langle B_z \rangle$ variation to $B_0 = 20 \pm 20$ G, and the semi-amplitude of the first harmonic to $B_1 = 1620 \pm 70$ G. We find $i + \beta = 139°$, with 1σ of uncertainties of $(+12°, -15°)$, which is qualitatively consistent with Shultz et al. (2017). Because ξ^1 CMa exhibits departures from a purely dipolar topology, we also produced a first harmonic fit to $\langle B_z \rangle$ (i.e. a dipole with a quadrupolar component; black dashed line). Both models assume an ephemeris of HJD$_0 = 2\,455\,220$ and a rotation period of 30 yr, consistent with the best-fit models from Shultz et al. (2017, 2018c).

The first harmonic fit is preferred based on its smaller residuals (Fig. 3b). The reduced χ^2 of the fundamental harmonic model is 34, with a *p*-value of effectively 0, indicating that the deviation from the best-fitting model is not due to statistical noise. The reduced χ^2 of the first harmonic model is 4.3, indicating a better fit to the data within the statistical possibility due to random noise (although, with a *p*-value of 10^{-4}, it is still not statistically compatible with a good fit).

We also calculated the Akaike information criterion (AIC) score (Akaike 1974) for each model, which considers the number of parameters and the goodness of fit against increased model complexity. The fundamental harmonic model yielded an AIC score of 295, while the first harmonic model produced an AIC score of 83. A lower AIC score indicates the first harmonic fit is the preferred model.

To evaluate the possibility that the uncertainty on $\langle B_z \rangle$ may have been underestimated, we repeated this test, increasing the error on the $\langle B_z \rangle$ curve by 50 per cent. In this case, the first harmonic model is statistically preferred (*p*-value = 0.075), and the fundamental harmonic model is still statistically excluded (with a *p*-value of effectively 0). The fundamental harmonic model yielded an AIC score of 162, and the first harmonic model produced an AIC score of 71, indicating that in the unlikely event the error bars were underestimated by 50 per cent due to unknown sources of systematic error, the conclusion that the first harmonic fit is preferred remains unchanged.

A caveat to this result is that the full rotation cycle of ξ^1 CMa has not yet been completely observed. It is likely that the magnetic topology is pre-dominantly dipolar, and the higher order components are small; however, the actual topological configuration cannot be determined at this point. This said, our results are *consistent* with the evidence for a complex field, provided by the analyses of the Stokes *V* profiles (Shultz et al. 2018c, and above). Further monitoring of the longitudinal field curve will be required in order to fully constrain the rotational period of ξ^1 CMa.

4 MAGNETOSPHERIC DIAGNOSTICS

The magnetic fields of O- and B-type stars trap the outflowing stellar wind and channel it into a circumstellar magnetosphere that co-rotates with the star. If the star is not rotating fast enough to provide sufficient centrifugal support to the plasma to overcome gravity, the confined wind material will fall back to the stellar surface under the influence of gravity on a dynamical time-scale, forming a 'Dynamical

---

[4]The term *crossover signature* is used to describe a Zeeman signature corresponding to the magnetic null. In contrast to the usual antisymmetric Zeeman signature, a crossover signature is symmetric about line centre and results from the distribution of Doppler shifts at the stellar surface.
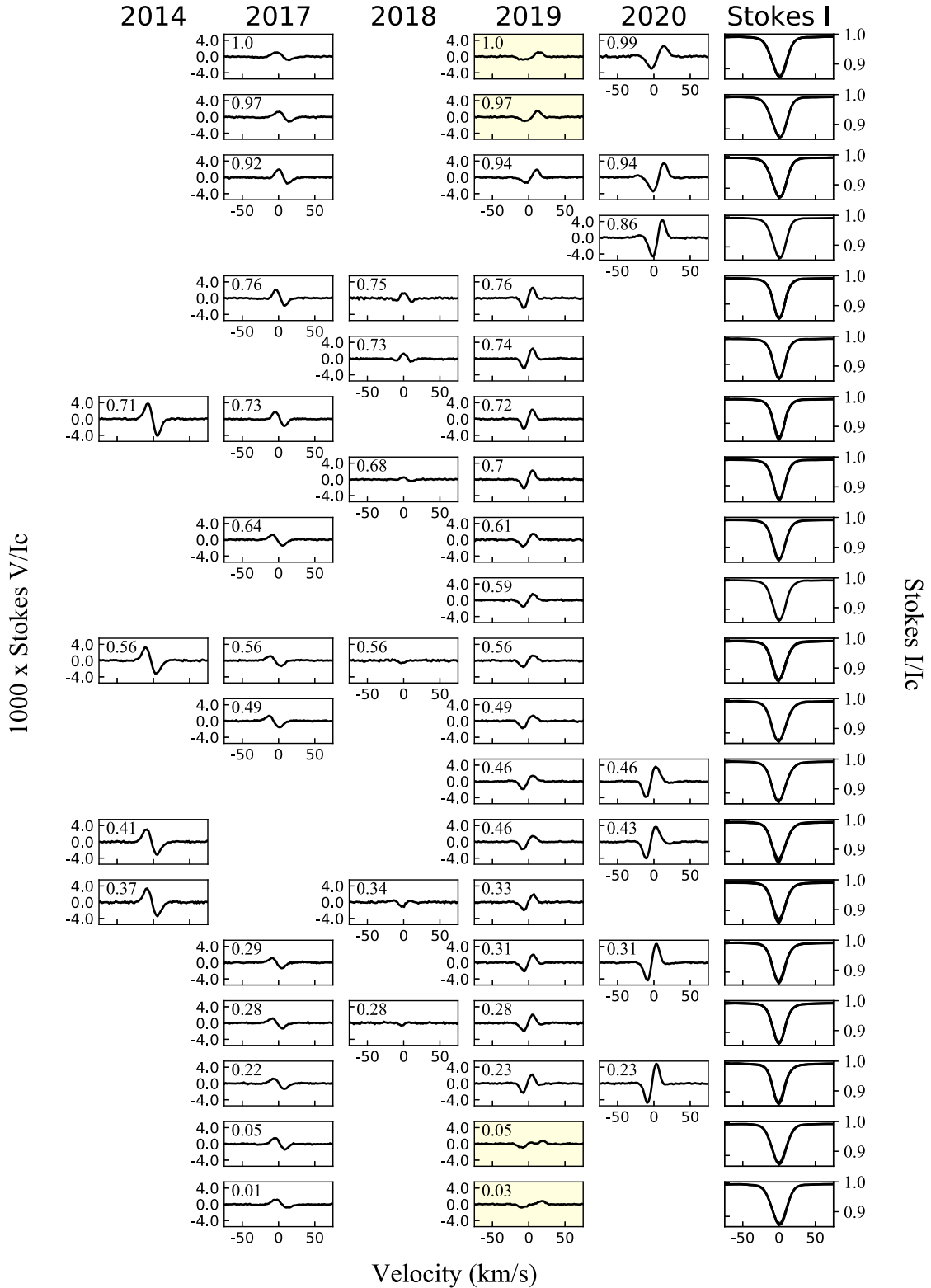
Figure 1. Stokes *V* and Stokes *I* profiles from several recent observational epochs, shifted to their central velocities, and arranged in order of increasing pulsation phase (indicated in the upper left-hand corner of each subplot). The 2019–2020 Stokes *V* profiles show negative Zeeman signatures, in contrast to the positive signatures in the 2014–2017 profiles, and the crossover signatures in the 2018 data set. We highlight (in yellow shading) the 2019 Stokes *V* profiles near pulsation phase 0.05 that have an unusual shape. The Stokes *I* profiles obtained at a given pulsation phase are identical between years.
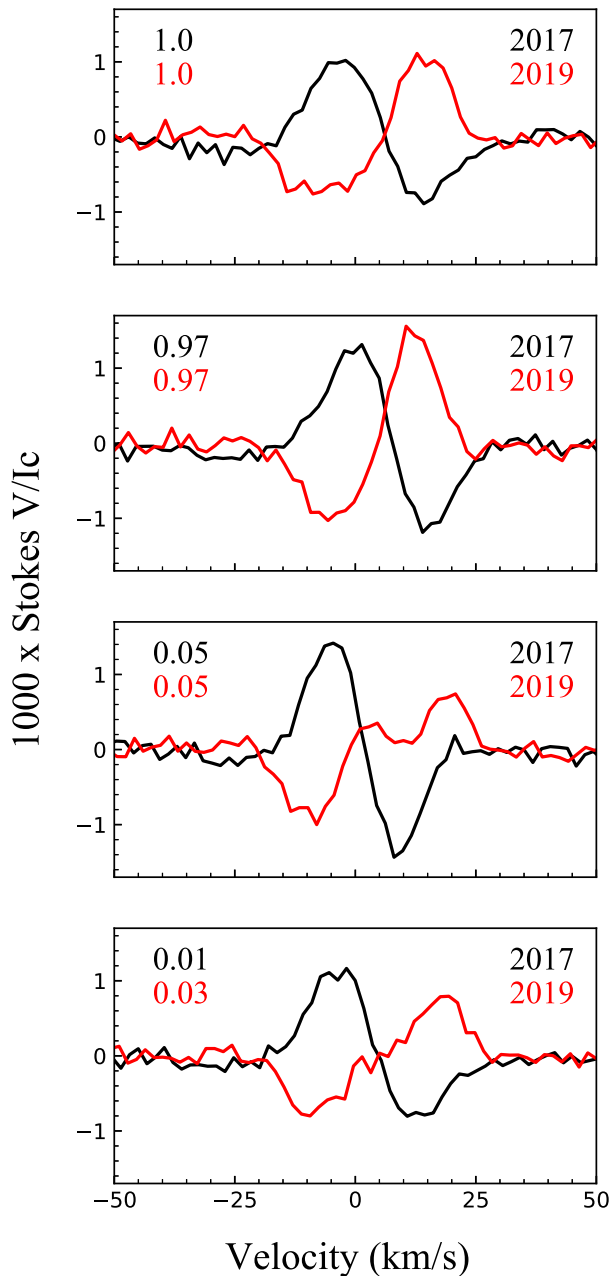
Figure 2. A close-up view of the four highlighted panels in Fig. 1. These Stokes *V* profiles from 2019 (red) have unusual shapes when compared to the Stokes *V* profiles from 2017 (black) at similar pulsation phase (indicated in the upper left-hand corner of each subplot).

Magnetosphere' (DM; Sundqvist et al. 2012; Petit et al. 2013). To date, ξ^1 CMa is the only magnetic B-type star observed to have Hα emission characteristic of originating within a DM (Shultz et al. 2017).

Since the magnetic axis is often inclined with respect to the stellar rotation axis, the magnetosphere can be viewed from different angles as the star rotates, leading to variability within the stellar spectrum. Wind-sensitive UV resonance lines (e.g. Si IV $\lambda\lambda$1393, 1402, C IV $\lambda\lambda$1548, 1550, and N V $\lambda\lambda$1238, 1242), as well as the Hα line, often bear signatures of this rotational modulation. For example, maximum (minimum) Hα emission typically corresponds with the

closest approach of the magnetic pole (equator) to an observer's line-of-sight. Such rotational modulation in UV lines has been observed (see e.g. Henrichs et al. 2013; Shultz et al. 2018a; David-Uraz et al. 2021) and modelled (see e.g. Marcolino et al. 2013; ud-Doula et al. 2013; Erba et al. 2020) in detail for both magnetic O- and B-type stars. We present here an analysis of the Hα emission of ξ^1 CMa and consider it in the context of the observed longitudinal field curve. We also examine the variability of the Si IV, C IV, and N V doublets in the UV spectra of ξ^1 CMa, and compare it to the rotational modulation visible in the UV spectra of the similar magnetic pulsator β Cep.

4.1 Hα emission

We calculated the equivalent width (EW) of the Hα line in the 2018–2020 observational epochs using an integration range of ± 0.4 nm about line centre. In order to provide a precise measurement of the variation in line strength, we renormalized the line profiles to a consistent continuum by fitting a line to the spectrum within 0.05 nm of the edge of the integration range, then dividing the profile by the line. These measurements are reported in Table C1. The EWs from 2000 to 2017 were previously published by Shultz et al. (2017).

Fig. 3(c) shows the variation of the Hα EW as a function of time. The Hα emission is modulated on the pulsation period, which introduces scatter outside the formal error bars in the measurements obtained at any given epoch (Shultz et al. 2017). We fit the annual weighted means (open circles) with a second harmonic sinusoidal model (solid black curve), using the same ephemeris as the fits to the $\langle B_z \rangle$ curve. Since both magnetic poles are visible, we expect the EW to follow a double-wave variation (see e.g. Shultz et al. 2020), requiring a minimum of two sinusoidal terms to fit. In practice we found that three terms were necessary to obtain a reasonable fit. While the Hα emission provides a well-sampled data set, it is almost guaranteed to be anharmonic due to its formation within ξ^1 CMa's magnetosphere. Therefore, a determination of the rotation period from an as-yet incomplete Hα timeseries is not strictly reliable.

Overall, the variation of the Hα emission shown in Fig. 3(c) is qualitatively consistent with the magnetic data. The minimum of the Hα EW (and therefore maximum Hα emission) corresponds with the maximum of $\langle B_z \rangle$; conversely, the null of $\langle B_z \rangle$ corresponds with the maximum Hα EW. This double wave variation is expected from a magnetosphere co-rotating with the star in which both poles are viewed. We expect to see an increase in the strength of the Hα emission as the negative pole approaches the line of sight.

Shultz et al. (2017) showed that the Hα emission profile is highly asymmetric, and that this asymmetry varies coherently with pulsation. They furthermore demonstrated that this could not be explained by the underlying pulsational variation of the photospheric line profile. As a measurement of emission profile asymmetry, we calculated the Hα V/R ratio as the ratio of the equivalent width of the blue side of the line to the equivalent width of the red side of the line, using the procedure from Shultz et al. (2017). We also applied a 3σ outlier rejection criterion to all data sets. The V/R ratio provides a quantitative assessment of pulsationally induced asymmetries in the line profile.

In Fig. 4, we show the Hα V/R variability as a function of pulsation phase. The data are separated by observational epoch, and the colors indicate proximity to the maximum of the longitudinal magnetic field (red, blue colors indicating proximity to $\langle B_{z,\,max} \rangle$, $\langle B_{z,\,min} \rangle$, respectively). We calculated the amplitudes of the V/R curve for each observational epoch using a least-squares first-order sinusoidal fit to the data; these are shown in Fig. 3d. The V/R amplitude varies sharply with $\langle B_z \rangle$. Figs 3d and 4 show that the
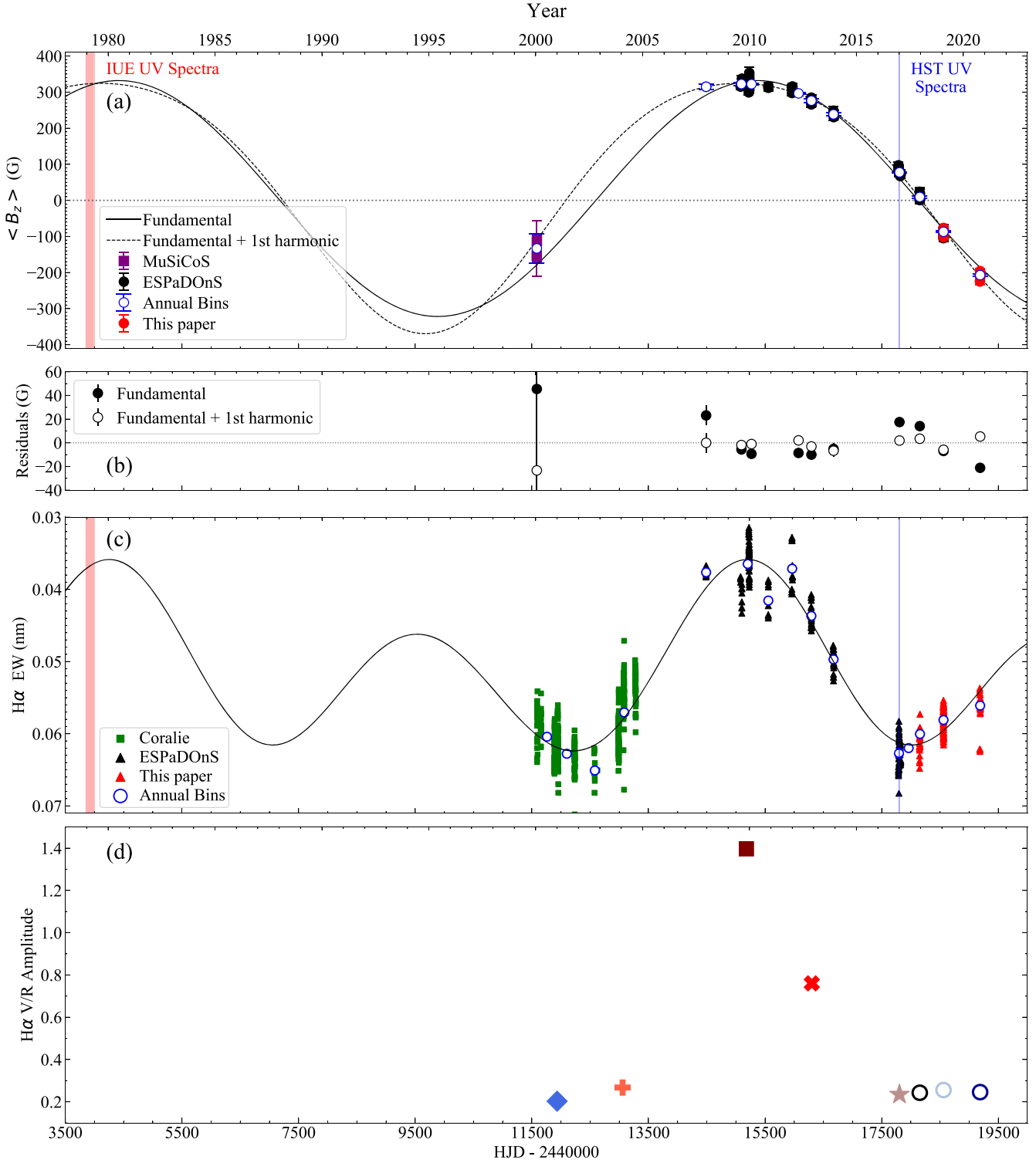
Figure 3. (a) $\langle B_z \rangle$ as a function of time. Previously reported observations (purple and black filled circles) are plotted alongside the new 2019–2020 data (red filled circles). The annually binned weighted means of $\langle B_z \rangle$ are indicated by the blue open circles. We also include two fits to the weighted means using a fundamental harmonic model (black solid line) and a first harmonic model (black dashed line). The vertical shading illustrates when the *IUE* and *HST* UV spectra were obtained. (b) Residuals for the fits to the $\langle B_z \rangle$ curve. (c) H α equivalent widths (EWs) as a function of time. The EWs from 2000 to 2017 were previously published by Shultz et al. (2017); EWs from 2018 to 2020 (in red filled triangles) are new to this paper. The annually binned weighted means of the H α EWs are marked in blue open circles. The black curve shows the best-fitting second harmonic model. (d) Amplitude of the H α V/R curve as a function of time. The data bins, colours, and symbols match the H α V/R curve shown in Fig. 4.
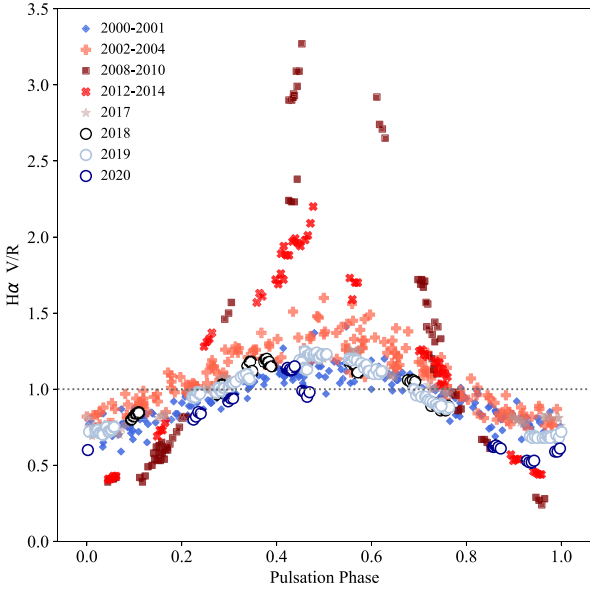
Figure 4. H α V/R as a function of pulsation phase. The symbols represent individual observing epochs, and the colour indicates proximity to the maximum of the observed longitudinal field curve (dark red is closer to $\langle B_{z, \max} \rangle$, dark blue is closer to $\langle B_{z, \min} \rangle$).

2008–2010 V/R curve has a considerably larger amplitude than any of the other V/R curves. This occurs at the positive extremum of $\langle B_z \rangle$ (Fig. 3a). However, from 2010–2013, the V/R curve amplitude sharply decreases while $\langle B_z \rangle$ decreases only slightly. The amplitudes of the V/R curve are still comparably small when the longitudinal field is measured near -200 G in the CORALIE data (2000) and the newly obtained ESPaDOnS data (2020). It appears that the amplitude of the V/R curve only changes significantly near the magnetic poles. We would therefore expect to observe a sharp increase in the V/R curve amplitude (of similar amplitude to the 2008–2010 data set) during the negative extremum of the longitudinal magnetic field. Continued monitoring will be needed to confirm this behaviour.

4.2 UV variability

As noted by Schnerr et al. (2008) and Shultz et al. (2017), the *IUE* UV emission spectra of ξ^1 CMa bear a strong resemblance to the archetypal magnetic β Cep pulsator β Cep (HD 205 021, B1 IV) in the N V, Si IV, and C IV doublets. β Cep exhibits a double-wave variation in its UV emission with a rotation period of 12 d (Henrichs et al. 1993, 2013). In this star, maximum emission occurs at rotation phases $\phi_{\mathrm{rot}} = 0$, 0.5 (corresponding with the extrema of the $\langle B_z \rangle$ curve), and minimum emission occurs at rotation phases $\phi_{\mathrm{rot}} = 0.25$, 0.75 (corresponding with the magnetic null).

An initial comparison of these two stars was presented by Schnerr et al. (2008), who showed the similarity of ξ^1 CMa's C IV doublet to that of β Cep, observed at maximum emission. A similar analysis, using the same (*IUE*) data as Schnerr et al. (2008), was given by Shultz et al. (2017) for the N V $\lambda\lambda$1238, 1242 and Al III $\lambda\lambda$1854, 1863 doublets. The authors came to a similar conclusion, emphasizing the strong resemblance between the *IUE* spectrum of ξ^1 CMa and β Cep's maximum emission state. Schnerr et al. (2008) highlighted that the *IUE* spectrum of ξ^1 CMa was obtained over a relatively small time-scale (approx. 7 h), and so it was unlikely that rotational variability would be observable in ξ^1 CMa's UV wind lines. Shultz
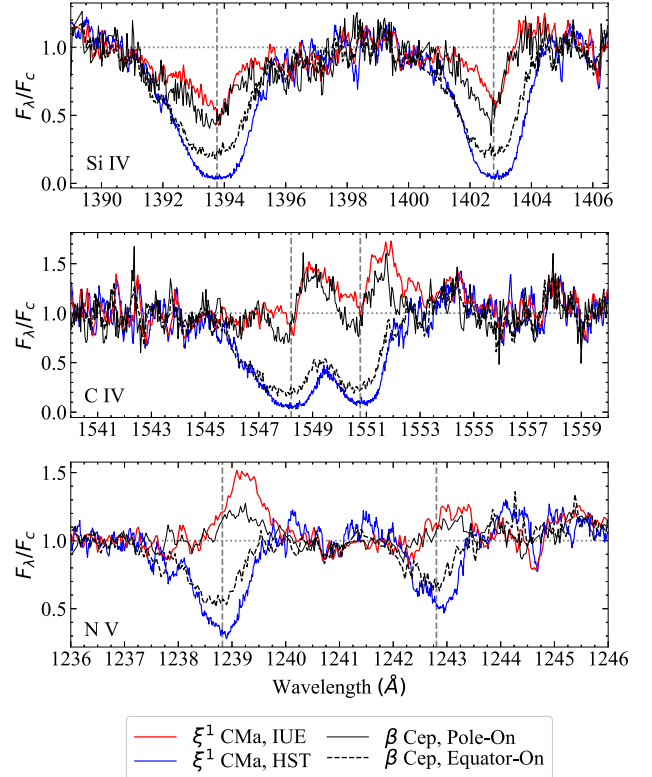

Figure 5. *IUE* and *HST* spectra (black dashed line and solid lines, respectively) of the Si IV, C IV, and N V wind-sensitive UV resonance lines of ξ^1 CMa, compared with *IUE* spectra of the same lines in β Cep, obtained at maximum (red lines) and minimum (blue lines) emission.

et al. (2017) proposed that this minimal variability resulted from an oblique dipole configuration with a long rotation period, and showed that the UV data for ξ^1 CMa were obtained near phase $\phi_{\mathrm{rot}} = 1.0$, assuming their best-fit 30 yr rotation period. This is illustrated in Figs 3(a) and (c), where we show the time of the *IUE* observation (red vertical bar), along with the projected longitudinal field curve assuming our sinusoidal fits with a rotation period of 30 yr.

Since the analysis of the *IUE* data by Schnerr et al. (2008) and Shultz et al. (2017), an additional set of UV spectra was obtained in 2017 using *HST* (Figs 3a and c, blue vertical bar). These data are consistent with the *IUE* observations having been obtained near magnetic maximum. In Fig. 5, we show the Si IV, C IV, and N V doublets for the *IUE* spectrum (red) and new *HST* spectrum (blue) of ξ^1 CMa, in conjunction with the UV spectra of β Cep obtained at maximum emission (a pole-on view of the magnetosphere; solid black lines) and minimum emission (an equator-on view of the magnetosphere; dashed black lines). In this figure, the *IUE* spectra of ξ^1 CMa have been coadded to produce a single, averaged spectrum that ignores smaller line profile variations due to pulsation. The same procedure was used for the *HST* spectra of ξ^1 CMa. Since the pulsational RV amplitude is much smaller than the line width, pulsational phase smearing in a given data set is negligible. Furthermore, each individual data set covers at least one pulsational cycle. The dramatic changes between the two data sets therefore cannot be due to pulsation, but must originate from rotation. We also note that in the *IUE* spectra, there is no statistically significant variation of the EW with pulsation. Therefore, the amplitude of line strength variation with pulsation is negligible compared with that due to rotation.

The UV spectra of ξ^1 CMa exhibit similar line profile morphologies to those of β Cep at the high and low states, corresponding to extrema and nulls of the $\langle B_z \rangle$ curve, respectively. From the ESPaDOnS spectropolarimetric data set (see Fig. 3a), we know the longitudinal field was $\langle B_z \rangle \sim 78$ G when the *HST* UV data were obtained, which is relatively close to magnetic null. Assuming a 30 yr rotation period for ξ^1 CMa, the *IUE* and *HST* spectra were observed approximately 1.25 rotational cycles apart, corresponding with a one-quarter cycle phase difference between the two sets of spectra. The *IUE* spectrum would then correspond with the positive extremum of $\langle B_z \rangle$ ($\phi_{\rm rot} \approx 1.0$ as predicted in Shultz et al. (2017), placing the *HST* spectrum near phase $\phi_{\rm rot} \approx 0.25$).

The resonance doublets of ξ^1 CMa shown in Fig. 5 also exhibit greater absorption (in the *HST* spectrum, blue lines) and emission (in the *IUE* spectrum, red lines) than those of β Cep. This could be due to ξ^1 CMa's stronger magnetic field (by about a factor of 4; Henrichs et al. 2013), or due to its higher effective temperature or larger mass loss rate. Such speculation only accounts for a few of the many factors that influence UV line formation (Erba et al. 2021). Further UV observations of ξ^1 CMa obtained at different rotational phases will be critical in order to fully characterize the variability of its UV spectral lines.

5 CONCLUSIONS

We report here the first two unambiguous detections of a negative magnetic field in ξ^1 CMa with amplitudes of $\langle B_z \rangle = -87 \pm 2$ G and $\langle B_z \rangle = -207 \pm 3$ G. This confirms that both of ξ^1 CMa's magnetic hemispheres are visible over a single rotational cycle. We show that a first harmonic fit to the longitudinal field curve produces better agreement with the data than a pure sinusoidal fit. However, the preferred fit falls short of statistical significance and cannot be taken as a final model, nor should it be interpreted as primary evidence for departures from a purely dipolar topology. Rather, it is consistent with a magnetic topology that is somewhat more complex than a pure dipole, as first suggested in Shultz et al. (2018c). Based on the first harmonic fit depicted in Fig. 3(a), we predict that the negative extremum of the longitudinal magnetic field will occur in late 2024. Continued, well-sampled spectropolarimetric monitoring will be critical to our ability to provide improved constraints on the rotational period and on the different magnetic topological models.

Even so, ξ^1 CMa is still one of the most slowly rotating hot magnetic stars identified to date. A number of A-type stars with similarly long rotation periods have been observed; however, their slow rotation is likely the result of their pre-main-sequence evolution (as evidenced by their lack of significant winds; see e.g. Stępień & Landstreet 2002; Mathys 2017). Alternatively, ξ^1 CMa's extremely slow rotation may be a consequence of the interplay between its main-sequence mass loss and magnetic field[5] (e.g. ud-Doula et al. 2009). ξ^1 CMa is therefore a prime target for detailed evolutionary modelling, to determine if there is a way to self-consistently understand the evolution of the star, its magnetic field, and its rotation.

The double-wave variation of the H α emission seen in the equivalent width curve is consistent with a view of the circum-

stellar magnetosphere in which the observer sees both magnetic poles. The emission line asymmetry is observed to vary sharply with $\langle B_z \rangle$, therefore a large increase in the amplitude of the V/R ratio should be observable during the negative extremum of the longitudinal magnetic field. Additional observations will also be an important step in ascertaining the long-term behaviour of the H α emission.

Variability in the 2019 Stokes *V* profiles near pulsation phase $\phi_{\rm p} = 0$ may arise from the interaction between the star's radial pulsations and complex magnetic field topology. ξ^1 CMa's purportedly complex field and long rotation period make it an intriguing, but challenging candidate for Zeeman Doppler Imaging (ZDI; Donati & Brown 1997; Piskunov & Kochukhov 2002), which would enable a more in-depth investigation of the interplay between the radial pulsations and the magnetic field, provided a well-sampled spectropolarimetric data set is available once the rotational period has been fully covered.

It is worth noting that while departures from a purely dipolar topology are detectable in ξ^1 CMa, this is likely due to the high precision of the available spectropolarimetric data. The large-scale field of ξ^1 CMa is still dominated by the dipolar component. This stands in contrast with other magnetic B-type stars such as τ Sco (HD 149 438, B0.2 V) and HD 37776 (B2 V), for which the higher-order moments of the field are dominant (see e.g. Thompson & Landstreet 1985; Donati et al. 2006; Donati & Landstreet 2009; Kochukhov et al. 2011; Kochukhov 2015; Kochukhov & Wade 2016).

We present the first new UV spectrum of ξ^1 CMa obtained in the last ~40 yr, observed during 2017 when the longitudinal field curve was approaching magnetic null. There is a striking difference between the new UV spectra and those obtained in 1978–1979, which did not exhibit any measurable change over the course of a year. The new UV data show a close similarity to the UV spectrum of β Cep obtained near minimum emission. As both magnetic poles are visible, this suggests that ξ^1 CMa should show a double-wave variation in its UV and H α emission. This can be confirmed with future monitoring efforts. If the magnetic field of ξ^1 CMa is indeed complex, examining rotational modulation in its spectra will be an important and interesting case study in the impact of magnetic fields on early B-type stars.

[5]Recent work (e.g. Shultz et al. 2019b; Takahashi & Langer 2021) has suggested the rotation periods of Ap stars also increase over time (as in hotter stars), which suggests that magnetic braking during the main-sequence evolutionary phase may also occur among this population.

Finally, the authors wish to thank the referee, Dr. Colin Folsom, for his insightful comments.

REFERENCES

Akaike H., 1974, IEEE Trans. Autom. Control, 19, 716
Baudrand J., Bohm T., 1992, A&A, 259, 711
David-Uraz A., Petit V., Shultz M. E., Fullerton A. W., Erba C., Keszthelyi Z., Seadrow S., Wade G. A., 2021, MNRAS, 501, 2677
Donati J. F., Brown S. F., 1997, A&A, 326, 1135
Donati J. F., Catala C., Wade G. A., Gallou G., Delaigue G., Rabou P., 1999, A&AS, 134, 149
Donati J. F., Landstreet J. D., 2009, ARA&A, 47, 333
Donati J. F., Semel M., Carter B. D., Rees D. E., Collier Cameron A., 1997, MNRAS, 291, 658
Donati J. F., Wade G. A., Babel J., Henrichs H. f., de Jong J. A., Harries T. J., 2001, MNRAS, 326, 1265
Donati J. F. et al., 2006, MNRAS, 370, 629
Erba C., Petit V., David-Uraz A., Fullerton A., 2020, in Wade G., Alecian E., Bohlender D., Sigut A., eds, Proceedings of the Polish Astronomical Society, Vol. 11, Stellar Magnetism: A Workshop in Honour of the Career and Contributions of John D. Landstreet, Polish Astronomical Society, Warsaw, Poland, p. 74, arXiv:1912.08748
Erba C. et al., 2021, MNRAS, preprint (arXiv:2106.13676)
Gies D. R., Lambert D. L., 1992, ApJ, 387, 673
Grunhut J. H. et al., 2017, MNRAS, 465, 2432
Henrichs H. F., 2001, in Mathys G., Solanki S. K., Wickramasinghe D. T., eds, ASP Conf. Ser. Vol. 248, Magnetic Fields Across the Hertzsprung-Russell Diagram. Astron. Soc. Pac., San Francisco, p. 393.
Henrichs H. F. et al., 1993, in Nemec J. M., Matthews J. M., eds, IAU Colloq. 139, New Perspectives on Stellar Pulsation and Pulsating Variable Stars. Cambridge University Press, Cambridge, UK, p. 186
Henrichs H. F. et al., 1998, in Wamsteker W., Gonzalez Riestra R., Harris B., eds, ESA Special Publication Vol. 413, Ultraviolet Astrophysics Beyond the *IUE* Final Archive. ESA, Noordwijk , p. 157
Henrichs H. F. et al., 2000, in Smith M. A., Henrichs H. F., Fabregat J., eds, ASP Conf.Ser. Vol. 214, IAU Colloq. 175: The Be Phenomenon in Early-Type Stars. Astron. Soc. Pac., San Francisco, p. 324.

Henrichs H. F. et al., 2012, A&A, 545, A119
Henrichs H. F. et al., 2013, A&A, 555, A46
Hubrig S., Briquet M., Schöller M., De Cat P., Mathys G., Aerts C., 2006, MNRAS, 369, L61
Hubrig S., Ilyin I., Schöller M., Briquet M., Morel T., De Cat P., 2011, ApJ, 726, L5
Järvinen S. P., Hubrig S., Schöller M., Ilyin I., 2018, New Astron., 62, 37
Kaper L., Henrichs H. F., Nichols J. S., Snoek L. C., Volten H., Zwarthoed G. A. A., 1996, A&AS, 116, 257
Kaper L., Henrichs H. F., Nichols J. S., Telting J. H., 1999, A&A, 344, 231
Keszthelyi Z., Meynet G., Georgy C., Wade G. A., Petit V., David-Uraz A., 2019, MNRAS, 485, 5843
Kochukhov O., 2015, A&A, 580, A39
Kochukhov O., Lundin A., Romanyuk I., Kudryavtsev D., 2011, ApJ, 726, 24
Kochukhov O., Wade G. A., 2016, A&A, 586, A30
Kupka F., Piskunov N., Ryabchikova T. A., Stempels H. C., Weiss W. W., 1999, A&AS, 138, 119
Kupka F. G., Ryabchikova T. A., Piskunov N. E., Stempels H. C., Weiss W. W., 2000, Balt. Astron., 9, 590
Marcolino W. L. F., Bouret J. C., Sundqvist J. O., Walborn N. R., Fullerton A. W., Howarth I. D., Wade G. A., ud-Doula A., 2013, MNRAS, 431, 2253
Massa D. et al., 1995, ApJ, 452, L53
Mathys G., 1989, Fund. Cosmic Phys., 13, 143
Mathys G., 2017, A&A, 601, A14
Morel T., Butler K., Aerts C., Neiner C., Briquet M., 2006, A&A, 457, 651
Morel T. et al., 2015, in Meynet G., Georgy C., Groh J., Stee P., eds, Proc. IAU Symp. 307, New Windows on Massive Stars. Kluwer, Dordrecht, p. 342.
Nazé Y., Ud-Doula A., Spano M., Rauw G., De Becker M., Walborn N. R., 2010, A&A, 520, A59
Neiner C., Geers V. C., Henrichs H. F., Floquet M., Frémat Y., Hubert A.-M., Preuss O., Wiersema K., 2003a, A&A, 406, 1019
Neiner C. et al., 2003b, A&A, 411, 565
Nichols J. S., Linsky J. L., 1996, AJ, 111, 517
Oskinova L. M., Nazé Y., Todt H., Huenemoerder D. P., Ignace R., Hubrig S., Hamann W.-R., 2014, Nat. Commun., 5, 4024
Petit V. et al., 2013, MNRAS, 429, 398
Petit V. et al., 2017, MNRAS, 466, 1052
Petit V. et al., 2019, MNRAS, 489, 5669
Piskunov N., Kochukhov O., 2002, A&A, 381, 736
Piskunov N. E., Kupka F., Ryabchikova T. A., Weiss W. W., Jeffery C. S., 1995, A&AS, 112, 525
Preston G. W., 1967, ApJ, 150, 547
Queloz D. et al., 2000, A&A, 354, 99
Queloz D. et al., 2001, The Messenger, 105, 1
Ryabchikova T., Piskunov N., Kurucz R. L., Stempels H. C., Heiter U., Pakhomov Y., Barklem P. S., 2015, Phys. Scr., 90, 054005
Ryabchikova T. A., Piskunov N. E., Kupka F., Weiss W. W., 1997, Balt. Astron., 6, 244
Saesen S., Briquet M., Aerts C., 2006, Commun. Asteroseismol., 147, 109
Schnerr R. S. et al., 2008, A&A, 483, 857
Shore S. N., 1987, AJ, 94, 731
Shultz M., Kochukhov O., Wade G. A., Rivinius T., 2018c, MNRAS, 478, L39
Shultz M., Rivinius T., Das B., Wade G. A., Chand ra P., 2019a, MNRAS, 486, 5558
Shultz M., Rivinius T., Wade G. A., Alecian E., Petit V., BinaMIcS Collaboration, 2018a, MNRAS, 475, 839
Shultz M., Wade G. A., 2017, MNRAS, 468, 3985
Shultz M., Wade G. A., Rivinius T., Neiner C., Henrichs H., Marcolino W., MiMeS Collaboration, 2017, MNRAS, 471, 2286
Shultz M. E. et al., 2018b, MNRAS, 475, 5144
Shultz M. E. et al., 2019b, MNRAS, 490, 274
Shultz M. E. et al., 2020, MNRAS, 499, 5379

Silvester J. et al., 2009, MNRAS, 398, 1505

Sohn S. T., et al. 2019, STIS Data Handbook v. 7.0, STScI, Baltimore

Stępień K., Landstreet J. D., 2002, A&A, 384, 554

Sundqvist J. O., ud-Doula A., Owocki S. P., Townsend R. H. D., Howarth I.
    D., Wade G. A., 2012, MNRAS, 423, L21

Takahashi K., Langer N., 2021, A&A, 646, A19

Thompson I. B., Landstreet J. D., 1985, ApJ, 289, L9

ud-Doula A., Owocki S. P., 2002, ApJ, 576, 413

ud-Doula A., Owocki S. P., Townsend R. H. D., 2009, MNRAS, 392, 1022

ud-Doula A., Sundqvist J. O., Owocki S. P., Petit V., Townsend R. H. D.,
    2013, MNRAS, 428, 2723

Wade G. A., Donati J. F., Landstreet J. D., Shorlin S. L. S., 2000, MNRAS,
    313, 851

Wade G. A. et al., 2016, MNRAS, 456, 2

Wade G. A. et al., 2020, MNRAS, 492, 2762

APPENDIX A: RADIAL VELOCITY MEASUREMENTS FROM ESPADONS OBSERVATIONS

Table A1. Radial velocity (RV) measurements obtained from the intensity spectra (that is, from the individual subexposures of the spectropolarimetric sequences) in 2020. RVs in 2019 were reported by Wade et al. (2020).

HJD - 2450000	RV (km s^{-1})	HJD - 2450000	RV (km s^{-1})
9183.04882	7.8 ± 0.8	9190.06625	39.4 ± 1.4
9183.04988	7.8 ± 0.8	9190.06732	39.4 ± 1.4
9183.05095	7.8 ± 0.8	9190.96474	20.6 ± 1.1
9183.05201	7.9 ± 0.8	9190.96581	19.9 ± 1.0
9183.99882	39.2 ± 1.4	9190.96687	19.4 ± 1.0
9183.99988	39.1 ± 1.4	9190.96794	19.1 ± 1.0
9184.00094	38.9 ± 1.4	9191.93559	36.0 ± 1.4
9184.00200	38.9 ± 1.4	9191.93665	36.3 ± 1.4
9187.02426	7.7 ± 0.8	9191.93772	36.5 ± 1.4
9187.02532	7.7 ± 0.8	9191.93878	36.8 ± 1.4
9187.02638	7.6 ± 0.8	9192.02799	13.7 ± 0.9
9187.02744	7.6 ± 0.8	9192.02905	13.3 ± 0.9
9190.06412	39.2 ± 1.4	9192.03011	12.8 ± 0.9
9190.06519	39.3 ± 1.4	9192.03118	12.6 ± 0.9

APPENDIX B: TABLE OF OBSERVATIONS WITH *HST*/STIS

Table B1. STIS spectroscopy of ξ^1 CMa (Program 14657, PI: Oskinova).

ObsID	UT (Start)	ExpTime (s)	MJD (mid)	SNR*
od6n07010	2017-02-17T00:04:47	228	57801.0046	6.4
od6n07020	2017-02-17T00:10:52	228	57801.0089	6.3
od6n07030	2017-02-17T00:15:04	228	57801.0118	6.3
od6n07040	2017-02-17T00:19:16	228	57801.0147	6.2
od6n07050	2017-02-17T00:23:28	228	57801.0176	6.1
od6n07060	2017-02-17T00:27:40	228	57801.0205	6.0
od6n07070	2017-02-17T00:31:52	218	57801.0234	5.7
od6n08010	2017-02-17T01:40:09	228	57801.0709	6.1
od6n08020	2017-02-17T01:46:14	228	57801.0751	6.1
od6n08030	2017-02-17T01:50:26	228	57801.0780	6.1
od6n08040	2017-02-17T01:54:38	228	57801.0809	6.0
od6n08050	2017-02-17T01:58:50	228	57801.0839	5.9
od6n08060	2017-02-17T02:03:02	228	57801.0868	5.9
od6n08070	2017-02-17T02:07:14	218	57801.0896	5.8
od6n09010	2017-02-17T03:15:30	228	57801.1371	6.1
od6n09020	2017-02-17T03:21:35	228	57801.1413	6.4
od6n09030	2017-02-17T03:25:47	228	57801.1442	6.3
od6n09040	2017-02-17T03:29:59	228	57801.1471	6.3
od6n09050	2017-02-17T03:34:11	228	57801.1501	6.4
od6n09060	2017-02-17T03:38:23	228	57801.1530	6.3
od6n09070	2017-02-17T03:42:35	218	57801.1558	6.3
od6n10010	2017-02-17T04:50:52	228	57801.2033	6.0
od6n10020	2017-02-17T04:56:57	228	57801.2075	6.2
od6n10030	2017-02-17T05:01:09	228	57801.2105	6.2
od6n10040	2017-02-17T05:05:21	228	57801.2134	6.3
od6n10050	2017-02-17T05:09:33	228	57801.2163	6.2
od6n10060	2017-02-17T05:13:45	228	57801.2192	6.0
od6n10070	2017-02-17T05:17:57	218	57801.2221	5.9
od6n11010	2017-02-17T06:26:13	228	57801.2695	5.5
od6n11020	2017-02-17T06:32:18	228	57801.2738	5.8
od6n11030	2017-02-17T06:36:30	228	57801.2767	5.9
od6n11040	2017-02-17T06:40:42	228	57801.2796	6.0
od6n11050	2017-02-17T06:44:54	228	57801.2825	6.0
od6n11060	2017-02-17T06:49:06	228	57801.2854	5.9
od6n11070	2017-02-17T06:53:18	218	57801.2883	5.8
od6n12010	2017-02-17T08:01:36	228	57801.3358	5.8
od6n12020	2017-02-17T08:07:41	228	57801.3400	6.1
od6n12030	2017-02-17T08:11:53	228	57801.3429	6.2
od6n12040	2017-02-17T08:16:05	228	57801.3458	6.3
od6n12050	2017-02-17T08:20:17	228	57801.3487	6.3
od6n12060	2017-02-17T08:24:29	228	57801.3517	6.3
od6n12070	2017-02-17T08:28:41	218	57801.3545	6.0

Note. * Median value per pixel between 1493 and 1497 Å.

APPENDIX C: H α EQUIVALENT WIDTHS FROM ESPADONS OBSERVATIONS

Table C1. H α equivalent widths from the 2018, 2019, and 2020 ESPaDOnS data sets.

HJD−2 458 000	EW (nm)	HJD−2 458 000	EW (nm)	HJD−2 458 000	EW (nm)
8148.75321	0.0614 ± 0.0006	8557.84529	0.0586 ± 0.0006	8560.72580	0.0605 ± 0.0004
8148.75429	0.0606 ± 0.0005	8557.84639	0.0592 ± 0.0004	8560.72690	0.0608 ± 0.0005
8148.75537	0.0605 ± 0.0005	8557.84869	0.0578 ± 0.0005	8560.76130	0.0594 ± 0.0003
8148.75645	0.0620 ± 0.0007	8557.84984	0.0576 ± 0.0005	8560.76242	0.0598 ± 0.0003
8148.97144	0.0618 ± 0.0006	8557.85100	0.0583 ± 0.0005	8560.76352	0.0601 ± 0.0004
8148.97252	0.0618 ± 0.0005	8557.85214	0.0589 ± 0.0004	8560.76463	0.0591 ± 0.0004
8148.9736	0.0623 ± 0.0003	8559.76216	0.0569 ± 0.0004	8563.74274	0.0584 ± 0.0005
8148.97468	0.0618 ± 0.0004	8559.76327	0.0567 ± 0.0005	8563.74385	0.0583 ± 0.0004
8150.79889	0.0640 ± 0.0008	8559.76438	0.0581 ± 0.0004	8563.74496	0.0577 ± 0.0004
8150.79997	0.0638 ± 0.0005	8559.76548	0.0562 ± 0.0004	8563.74607	0.0579 ± 0.0005
8150.80105	0.0631 ± 0.0006	8559.76721	0.0574 ± 0.0005	8564.84618	0.0569 ± 0.0003
8150.80213	0.0648 ± 0.0006	8559.76837	0.0569 ± 0.0003	8564.84728	0.0573 ± 0.0004
8153.85512	0.0604 ± 0.0006	8559.76953	0.0570 ± 0.0004	8564.84839	0.0583 ± 0.0003
8153.8562	0.0601 ± 0.0006	8559.77068	0.0566 ± 0.0005	8564.84949	0.0578 ± 0.0005
8153.85728	0.0605 ± 0.0007	8559.77267	0.0570 ± 0.0004	8564.85109	0.0580 ± 0.0004
8153.85835	0.0593 ± 0.0004	8559.78286	0.0566 ± 0.0005	8564.85220	0.0573 ± 0.0004
8154.70789	0.0597 ± 0.0008	8559.78396	0.0559 ± 0.0004	8564.85331	0.0571 ± 0.0003
8154.70898	0.0601 ± 0.0009	8559.78506	0.0564 ± 0.0004	9183.04882	0.0537 ± 0.0006
8154.71008	0.0591 ± 0.0010	8559.78616	0.0562 ± 0.0004	9183.04988	0.0555 ± 0.0005
8154.71119	0.0600 ± 0.0007	8559.78814	0.0566 ± 0.0005	9183.05095	0.0543 ± 0.0003
8154.91334	0.0614 ± 0.0009	8559.78928	0.0563 ± 0.0006	9183.05201	0.0540 ± 0.0004
8154.91444	0.0607 ± 0.0010	8559.79043	0.0563 ± 0.0005	9183.99882	0.0624 ± 0.0006
8154.91554	0.0608 ± 0.0007	8559.79158	0.0572 ± 0.0005	9183.99988	0.0621 ± 0.0006
8154.91664	0.0606 ± 0.0009	8559.79356	0.0563 ± 0.0005	9184.00094	0.0622 ± 0.0006
8156.76397	0.0593 ± 0.0006	8559.79471	0.0562 ± 0.0004	9184.00200	0.0622 ± 0.0006
8156.76505	0.0595 ± 0.0006	8559.79586	0.0569 ± 0.0005	9187.02426	0.0546 ± 0.0003
8156.76613	0.0573 ± 0.0006	8559.79702	0.0568 ± 0.0005	9187.02532	0.0555 ± 0.0004
8156.76721	0.0600 ± 0.0005	8559.81117	0.0560 ± 0.0004	9187.02638	0.0553 ± 0.0004
8156.91427	0.0618 ± 0.0006	8559.81230	0.0563 ± 0.0005	9187.02744	0.0546 ± 0.0003
8156.91535	0.0604 ± 0.0005	8559.81342	0.0557 ± 0.0004	9190.06412	0.0563 ± 0.0008
8156.91643	0.0617 ± 0.0005	8559.81455	0.0554 ± 0.0005	9190.06519	0.0564 ± 0.0007
8557.76676	0.0594 ± 0.0005	8559.82356	0.0561 ± 0.0004	9190.06625	0.0563 ± 0.0007
8557.76787	0.0593 ± 0.0005	8559.82467	0.0559 ± 0.0003	9190.06732	0.0564 ± 0.0007
8557.76897	0.0600 ± 0.0006	8559.82577	0.0571 ± 0.0003	9190.96474	0.0572 ± 0.0004
8557.77007	0.0591 ± 0.0004	8559.82688	0.0563 ± 0.0003	9190.96581	0.0571 ± 0.0004
8557.7724	0.0599 ± 0.0006	8560.71247	0.0603 ± 0.0005	9190.96687	0.0570 ± 0.0004
8557.77349	0.0599 ± 0.0006	8560.71357	0.0607 ± 0.0006	9190.96794	0.0561 ± 0.0003
8557.77459	0.0601 ± 0.0005	8560.71467	0.0603 ± 0.0004	9191.93559	0.0564 ± 0.0006
8557.77569	0.0606 ± 0.0005	8560.71577	0.0612 ± 0.0004	9191.93665	0.0565 ± 0.0004
8557.83743	0.0588 ± 0.0005	8560.71862	0.0615 ± 0.0004	9191.93772	0.0566 ± 0.0006
8557.83856	0.0584 ± 0.0005	8560.71973	0.0605 ± 0.0004	9191.93878	0.0567 ± 0.0005
8557.83969	0.0596 ± 0.0004	8560.72083	0.0598 ± 0.0004	9192.02799	0.0551 ± 0.0004
8557.84081	0.0591 ± 0.0005	8560.72193	0.0603 ± 0.0004	9192.02905	0.0563 ± 0.0004
8557.84309	0.0586 ± 0.0004	8560.72359	0.0611 ± 0.0004	9192.03011	0.0560 ± 0.0004
8557.84419	0.0575 ± 0.0005	8560.72470	0.0606 ± 0.0003		

This paper has been typeset from a TEX/LATEX file prepared by the author.